



# Importance of the inlet air velocity on the establishment of flameless combustion in a laboratory combustor

A.S. Veríssimo, A.M.A. Rocha, M. Costa\*

Mechanical Engineering Department, Instituto Superior Técnico, Technical University of Lisbon, Lisbon, Portugal

## ARTICLE INFO

### Article history:

Received 11 April 2012

Received in revised form 16 May 2012

Accepted 29 May 2012

Available online 9 June 2012

### Keywords:

Experimental  
Flameless combustion  
Inlet air velocity  
OH<sup>\*</sup> radical  
Pollutant emissions

## ABSTRACT

This article examines the importance of the inlet air velocity ( $V_{\text{air}}$ ) on the establishment of flameless combustion in a 10 kW laboratory scale combustor. Variations in  $V_{\text{air}}$  were accomplished by changing the air nozzle diameter while maintaining constant all remaining input parameters. Initially, laser-Doppler anemometry was employed to evaluate the combustor flow aerodynamics under non-reacting conditions. Subsequently, flue-gas composition data and hydroxyl radical chemiluminescence (OH<sup>\*</sup>) imaging were obtained as a function of  $V_{\text{air}}$ . For two of these combustor operating conditions, spatial distributions of temperature, recorded with fine wire thermocouples, and of O<sub>2</sub>, CO<sub>2</sub>, unburned hydrocarbons, CO and NO<sub>x</sub> concentrations, measured with the aid of a sampling probe, were also obtained. The OH<sup>\*</sup> images showed that as  $V_{\text{air}}$  increases at a constant excess air coefficient ( $\lambda$ ) of 1.3, the main reaction zone, typical of flameless combustion condition, remains approximately in the same region of the combustor, because of the flow aerodynamics similarity, but the OH<sup>\*</sup> intensities decrease, which indicates higher entrainment ratios of the fuel and burned gases by the central air jet. For  $\lambda$  greater than 1.7, however, flameless oxidation could not be established regardless of the air jet momentum. This suggests that the establishment of the flameless combustion condition in future gas turbines through the dilution of the reactants with a substantial amount of flue gases in configurations where the combustion air is provided by a central high-momentum air jet that is surrounded by a number of low-momentum fuel jets may be problematic.

© 2012 Elsevier Inc. All rights reserved.

## 1. Introduction

Under flameless oxidation conditions combustion takes place in a distributed reaction zone rather than in a thin flame front, with relatively uniform and low temperatures and temperature fluctuations, in comparison to conventional flames. The fuel is oxidized in an environment that contains a significant amount of flue gases and a low concentration of oxygen, as a result of internal or external exhaust gas recirculation. The radiative heat fluxes are relatively high and uniform, there is no visible flame, the level of noise is low, soot formation is negligible and NO<sub>x</sub> and CO emissions are very low.

Flameless combustion is a technology relatively well established for industrial applications where heat is extracted from within the furnace while processing material, and is among the most promising technologies that can meet the stringent demands of reduced pollution and increased efficiency in future gas turbines. Gas turbine would operate lean adiabatic combustion (high oxygen content) while furnaces feature higher equivalence ratio (low oxygen content) [1]. This may pose difficulties in establishing

the flameless combustion regime in gas turbines. In this case, there is a need to recirculate, by aerodynamic means, a large amount of hot combustion products, with a relatively high oxygen content, which can make difficult to establish the proper reactants dilution for the onset of the flameless combustion condition. For instance, Li et al. [2] examine this combustion mode in a gas turbine combustor operating at atmospheric conditions. They found that the flameless combustion mode occurred only for a limited range of conditions at fuel lean conditions, high preheat temperature and high air flow rates.

Very recently [3], we examined the operational, combustion and emission characteristics of a small-scale combustor as a function of the excess air coefficient ( $\lambda$ ), which implied also changes in the inlet air velocity ( $V_{\text{air}}$ ). We observed that for  $\lambda$  below 1.5 it was possible to establish the flameless combustion regime, while for higher  $\lambda$  the fuel oxidation occurred in a conventional lean combustion mode. Due to the burner configuration, it was not possible to analyze independently the importance of  $\lambda$  and  $V_{\text{air}}$  on the combustion regime. In the present article we examine separately the effect of  $V_{\text{air}}$  on the establishment of flameless combustion.

Review articles on flameless combustion, also called flameless oxidation, moderate or intense low oxygen dilution (MILD) combustion, high temperature air combustion or colorless distributed combustion, include those of Wüning and Wüning [4], Cavaliere

\* Corresponding author.

E-mail address: [mcosta@ist.utl.pt](mailto:mcosta@ist.utl.pt) (M. Costa).

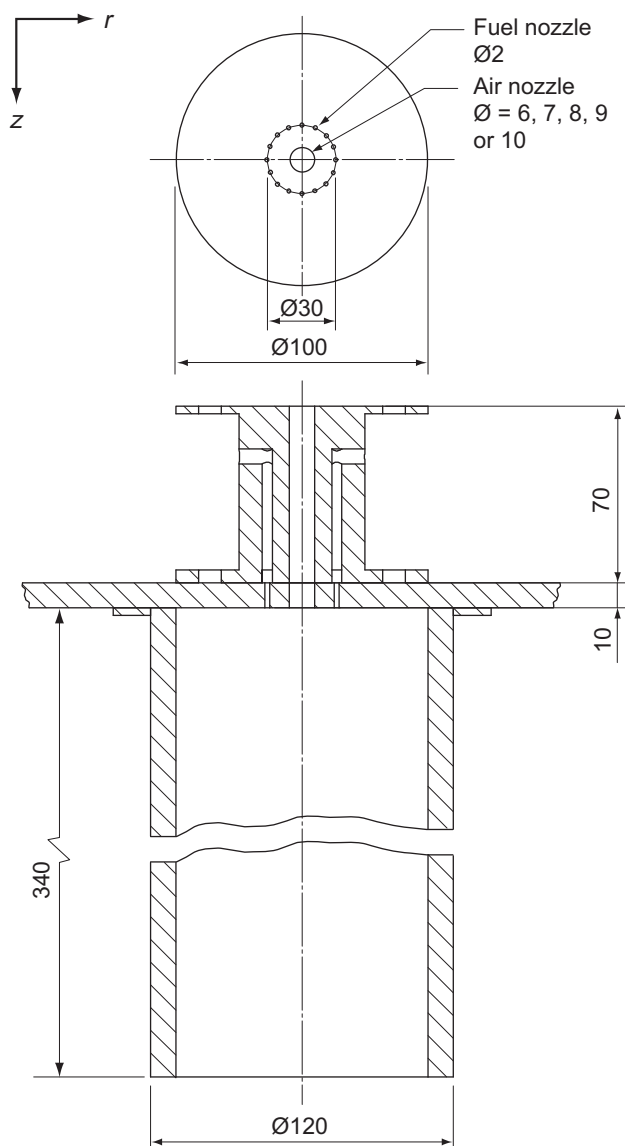


Fig. 1. Schematic of the combustor.

Table 1

Test conditions used to characterize the flow inside the combustor under non-reacting conditions.<sup>a</sup>

Run	Air nozzle diameter (mm)	$V_{\text{air}}$ (m/s)
1i	10	48.1
2i	7	98.2
3i	6	133.7

<sup>a</sup> For all conditions: inlet fuel (air) velocity = 6.2 m/s, air mass flow rate =  $4.4 \times 10^{-3}$  kg/s, inlet air temperature = 25 °C.

and de Joannon [5] and Tsuji et al. [6]. The effect of the initial air–fuel jet momentum on the establishment of flameless combustion has been studied by a number of investigators [7–13]. Szegő et al. [10] found that a certain fuel jet momentum threshold was needed to achieve flameless combustion conditions in a recuperative furnace. This momentum ensured the penetration of the fuel jets to a region classified as the oxidation zone. Also in a recuperative furnace, Mi et al. [11] reported an investigation on the importance of the initial air–fuel injection momentum rate and the air–fuel premixing on flameless combustion. The authors concluded,

numerically, that there is a critical momentum rate of the inlet fuel–air mixture below which the flameless combustion cannot occur. Also, they found, both experimentally and numerically, that, above this critical rate, both the momentum rate and the inlet fuel–air mixedness affect only marginally the stability of and emissions from the flameless combustion. In combustors other than recuperative furnaces, Mancini et al. [7] and Derudi et al. [8] also evidenced the threshold below which flameless combustion cannot occur not only for gaseous hydrocarbon fuels but also for highly reactive fuels, as hydrogen-containing fuel mixtures.

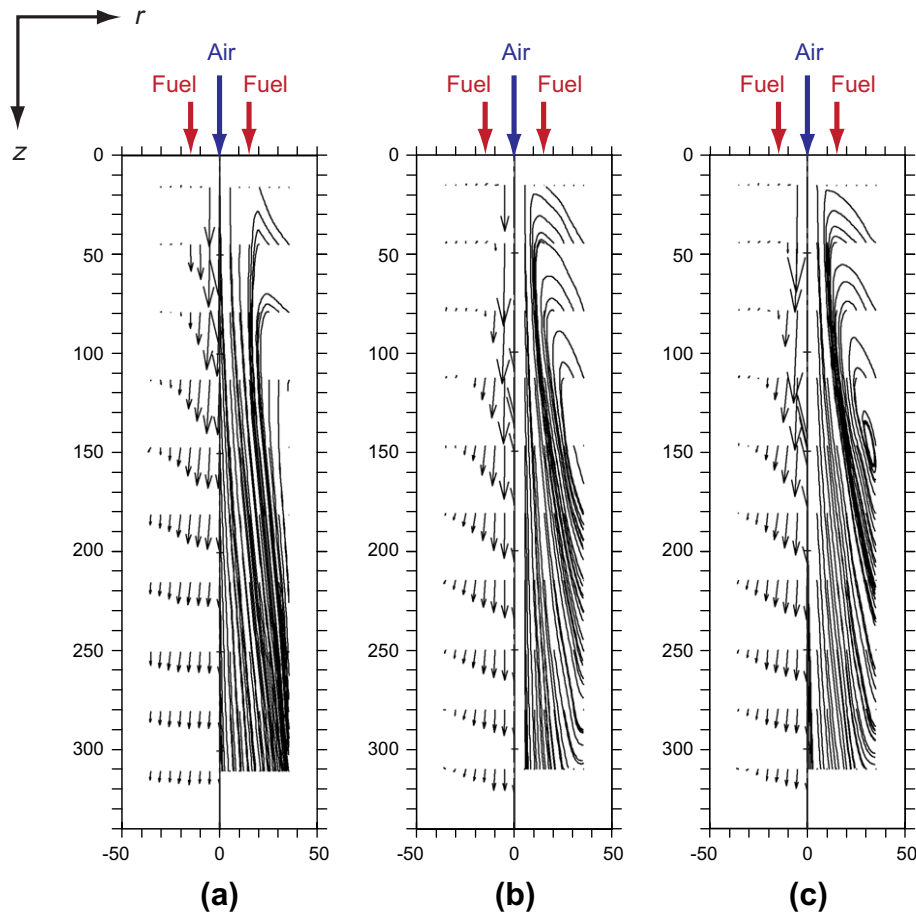
## 2. Materials and methods

Fig. 1 shows a schematic of the combustor used in this study. The combustion chamber is a quartz-glass cylinder with an inner diameter of 100 mm and a length of 340 mm. During the tests, the quartz cylinder was well-insulated with a 30-mm-thick ceramic fiber blanket. The burner is placed at the top end of the combustion chamber and the exhaustion of the burned gases is made by the bottom end through a convergent nozzle with a length of 150 mm and an angle of 15°. As seen in Fig. 1, the burner consists of a central orifice with a variable inner diameter (6, 7, 8, 9 and 10 mm in this study), through which the combustion air is supplied, surrounded by 16 small orifices of 2 mm inner diameter each, positioned on a circle with a radius of 15 mm, for the fuel (methane) supply. The combustion air is preheated by an electrical heating system.

A two-component velocimeter from Dantec™, which was operated in the dual-beam backward-scatter mode, was employed to characterize the flow inside the combustor under non-reacting conditions. This was accomplished in a combustor similar to that represented in Fig. 1, but made of stainless steel with two opposed rectangular quartz windows (320 × 90 mm) for optical access. Data rates of 0.5 kHz were obtained by seeding the flow with 1 µm alumina particles. The back-scattered light from the particles was collected by a fiber-optics probe with a beam separation of 38 mm and a focal length of 400 mm. Subsequently, the analog signal from the photomultipliers was band-pass filtered and processed by two Dantec™ 57N20/57N35 Burst Spectrum Analyzers interfaced with a personal computer, using “burst” data collection mode and a record length of 32 samples per burst. Velocity statistics were evaluated by ensemble averaging, calculated from 10,000 samples, using BURSTware software. Errors incurred in the measurement of velocities by displacement and distortion of the measuring volume due to refraction on the combustor model side walls (10 mm thick optical quartz glass windows) were negligible.

The data acquisition techniques used in the combustion tests along with the associated uncertainties are fully described in Verissimo et al. [3]. Local mean temperature measurements were obtained using 76 µm diameter fine wire platinum/platinum:13% rhodium (type R) thermocouples. The uncertainty due to radiation heat transfer was estimated to be less than 5% by considering the heat transfer by convection and radiation between the thermocouple bead and the surroundings.

The sampling of the gases for the measurement of local mean  $O_2$ ,  $CO_2$ , unburned hydrocarbons (HC), CO and  $NO_x$  concentrations was achieved using a stainless steel water-cooled probe. The analytical instrumentation included a magnetic pressure analyzer for  $O_2$  measurements, a non-dispersive infrared gas analyzer for  $CO_2$  and CO measurements, a flame ionization detector for HC measurements and a chemiluminescent analyzer for  $NO_x$  measurements. Quenching of the chemical reactions was found adequate, but no attempt was made to quantify the probe flow disturbances. On average, the repeatability of the gas species concentration data was within 10%. Flue-gas composition data, obtained at the begin-



**Fig. 2.** Mean velocity vectors and streamlines at the combustor symmetry plane for three  $V_{\text{air}}$  under non-reacting conditions. (a) Run 1i ( $V_{\text{air}} = 48.1$  m/s), (b) run 2i (98.2 m/s), and (c) run 3i (133.7 m/s).

**Table 2**  
Combustor operating conditions.<sup>a</sup>

Run	Air nozzle diameter (mm)	$V_{\text{air}}$ (m/s)	Inlet air momentum (N) <sup>b</sup>
1 <sup>c</sup>	10	113.2	0.5
2	9	138.2	0.6
3	8	176.8	0.8
4 <sup>c</sup>	7	230.1	1.1
5	6	311.0	1.4

<sup>a</sup> For all conditions: fuel thermal input = 10 kW, inlet fuel velocity = 6.2 m/s, inlet air temperature = 400 °C,  $\lambda = 1.3$ .

<sup>b</sup> Inlet air momentum = air mass flow rate  $\times V_{\text{air}}$ .

<sup>c</sup> Conditions for which measurements of local mean gas temperatures and local mean major gas species concentrations throughout the combustor have been carried out.

ning of the exhaust duct, were obtained using the same methods used for the concentration measurements inside the combustor. At the combustor exit, probe effects were negligible and errors arose mainly from quenching of chemical reactions, which was also found adequate. Repeatability of the flue-gas data was, on average, within 5% of the mean value.

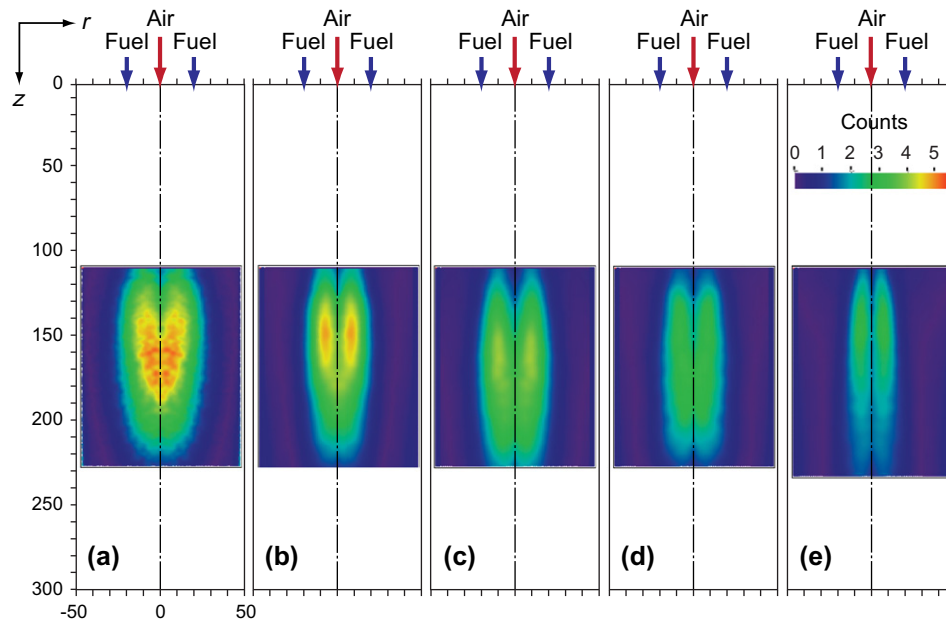
The OH\* images were collected on an ICCD camera (FLAMESTAR II, LaVision, 286  $\times$  384 pixels), equipped with an UV lens (UV Nikkor, 105 mm, f/4.5) and a bandpass interference filter (Melles Griot) centered at 310 nm with a bandwidth of 10 nm. In all chemiluminescence experiments, 500 single instantaneous images were recorded and averaged. The signal-to-noise ratio of the instantaneous images was better than 8:1. The ICCD camera collected the

signal from the entire combustion chamber so that the signals were spatially integrated in depth. In order to obtain local information instead of line-of-sight information, each averaged OH\* image was subsequently tomographically reconstructed using the inverse transform of Abel.

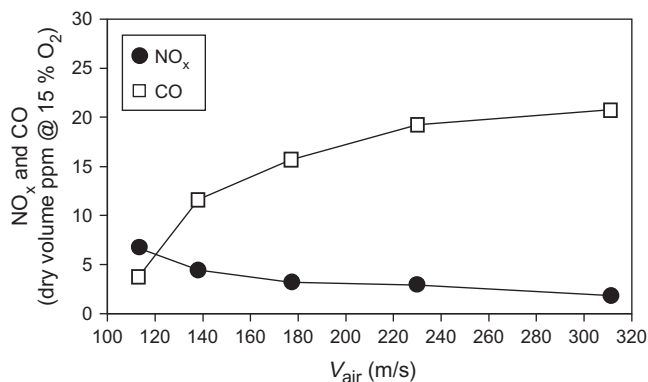
### 3. Results and discussion

Table 1 presents the test conditions used to characterize the flow inside the combustor under non-reacting conditions and Fig. 2 shows the mean velocity vectors and streamlines at the combustor symmetry plane for these conditions. In-plane velocities were quantified at 100 points, but the very near burner region was not covered as a result of restrictions imposed to optical access by structural restraints. It is seen that the central air jet momentum is large enough to generate a strong reverse flow zone that recirculates air back towards the near burner region, which is decisive to establish flameless combustion in the present configuration. The center of the recirculation zone is located at approximately the same position for the three cases. In contrast, as expected, the mean velocities increase as  $V_{\text{air}}$  increases.

In this investigation the variations in  $V_{\text{air}}$  were accomplished by changing the air nozzle diameter while maintaining constant all remaining input parameters, namely the air mass flow rate. This implies that, under reacting conditions, the entrainment ratio of the fuel and burned gases increases as  $V_{\text{air}}$  increases (the entrainment ratio generally varies as  $\approx 1/\text{nozzle diameter}$ ), which is critical for the onset of the flameless combustion condition.



**Fig. 3.** Mean OH\* images at the combustor symmetry plane for various  $V_{\text{air}}$  at a constant  $\lambda$  of 1.3. (a) run 1 ( $V_{\text{air}} = 113.2$  m/s), (b) run 2 (138.2 m/s), (c) run 3 (176.8 m/s), (d) run 4 (230.1 m/s), and (e) run 5 (311.0 m/s).



**Fig. 4.**  $\text{NO}_x$  and CO emissions as a function of  $V_{\text{air}}$  at a constant  $\lambda$  of 1.3.

Table 2 summarizes the test conditions used in this study. Methane (purity 99.5%) was used as fuel. Flue-gas measurements and OH\* imaging were obtained for all runs listed in Table 2, and detailed measurements of local mean gas temperatures and local mean major gas species concentrations were performed for runs 1 and 4.

Fig. 3 displays mean OH\* images at the combustor symmetry plane for various  $V_{\text{air}}$  (runs 1–5 in Table 2). Note that, due to the short lifetime of OH\*, the chemiluminescence originates only from the reaction zone so that this technique yields information about the position and size of the reaction zone [14]. The main reaction zone, as typified by the OH\* distribution, is located practically in the same region for all flames studied, between  $z \approx 110$  and 210–240 mm, depending on the specific condition. This is because the flow aerodynamics, particularly the location and extension of the recirculation zone, are analogous for all conditions studied, as suggested by the non-reacting data in Fig. 2. As  $V_{\text{air}}$  (and, consequently, the initial central air jet momentum) increases, the OH\* intensities decrease, which indicates higher entrainment ratios of the fuel and burned gases by the central air jet.

It is interesting to recall that in our previous work [3], as the  $\lambda$  (and, consequently,  $V_{\text{air}}$ ) increased, the main reaction zone moved progressively closer to the burner due to the faster entrainment of the fuel and burnt gases combined with the higher oxygen concentration in the recirculated flue-gas. Moreover, it was observed that above  $\lambda \approx 1.5$ , a flame front located at the strong shear region between the central jet and the external recirculation zone was established.

In order to evaluate if the present configuration allows the establishment of flameless combustion at high  $\lambda$  we conducted experiments as those reported here for  $\lambda = 1.5$  and 1.7 (not shown here) and, indeed, we observed the onset of the flameless combustion condition for higher  $\lambda$  above higher critical air jet momenta, depending upon the excess air level. However, we also observed that above  $\lambda = 1.7$ , flameless oxidation could not be established regardless of the air jet momentum. We shall return to this below.

Fig. 4 shows the  $\text{NO}_x$  and CO emissions as a function of  $V_{\text{air}}$ . HC emissions were not detected for any of the test conditions. Very low emissions were measured: specifically,  $\text{NO}_x$  emissions below 7 ppm@15%  $\text{O}_2$  and CO emissions below 21 ppm@15%  $\text{O}_2$ , regardless of the value of  $V_{\text{air}}$ . Fig. 4 reveals that the  $\text{NO}_x$  emissions gradually decrease and the CO emissions increase as  $V_{\text{air}}$  increases as a consequence of the impact of the increased entrainment ratios of the fuel and burned gases that induce faster and stronger dilution of the combustion air.

Fig. 5 shows the contours of temperature and  $\text{O}_2$ ,  $\text{CO}_2$ ,  $\text{NO}_x$ , HC and CO concentrations at the combustor symmetry plane for runs 1 and 4 in Table 2 (see also Fig. 3a and d). In Fig. 5, the left-hand side of each illustration corresponds to run 1 and the right-hand side to run 4. In the experiments, measurements of temperature and gas species concentration were undertaken at 100 points, as schematically represented on the top-left of Fig. 5.

The temperature fields are consistent with the main reaction zones identified through the OH\* images (see Fig. 3a and d), where the temperature reaches its maxima values around 1530 °C for run 1 and 1450 °C for run 4. In order to assess the uniformity of the temperature field, Fig. 6 shows the contours of the normalized temperature variation ( $T^*$ ) at the combustor symmetry plane for

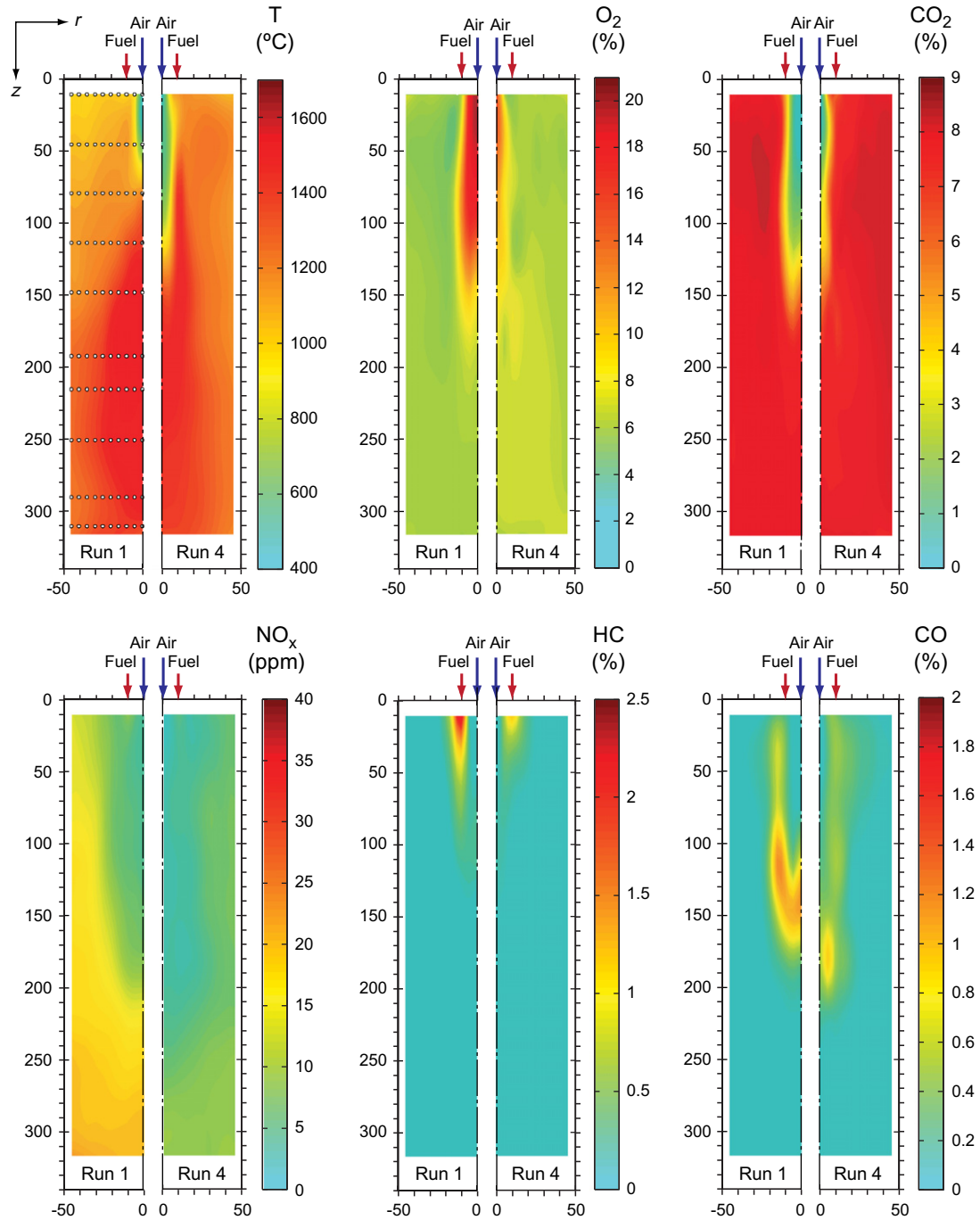


**Fig. 5.** Contours of temperature and  $O_2$ ,  $CO_2$ , HC, CO and  $NO_x$  concentrations at the combustor symmetry plane for runs 1 ( $V_{air} = 113.2$  m/s) and 4 (230.1 m/s).

runs 1 and 4. The normalized temperature variation  $T^*$  is defined as:

$$T^* = \frac{|T_{measured} - \bar{T}|}{\bar{T}} \quad (1)$$

where  $T_{measured}$  is the measured local temperature and  $\bar{T}$  is the average of all measured local temperatures in each run ( $\bar{T} = 1240^\circ\text{C}$  for run 1 and  $\bar{T} = 1233^\circ\text{C}$  for run 4). The degree of homogeneity is quite acceptable for both runs, as expected from the considerations above.

Fig. 5 also reveals that the chemistry fields are consistent with the main reaction zones identified through the  $OH^*$  images (see

Fig. 3a and d). In both runs, the highest concentrations of HC appear in front of the fuel entrance orifices (Fig. 5), but its presence along the combustor up to axial distances beyond  $z = 200$  mm for both runs reveals slower combustion. Consistently with the location of the main reaction zone, as identified by the  $OH^*$  imaging, the highest CO concentrations appear in the region  $110 < z < 210$  mm (Fig. 5) for run 1 and  $110 < z < 235$  mm (Fig. 5) for run 4, with a maximum of about 1% being reached at  $z \approx 150$  mm and  $r = 0$  for run 1 and of about 0.9% being reached at  $z \approx 180$  mm and  $r = 5$  mm for run 4.

The  $NO_x$  concentrations in both runs are low throughout the entire combustion chamber (Fig. 5), which is consistent with the comparable  $NO_x$  emissions (Fig. 4). Fig. 5 shows a progressive in-



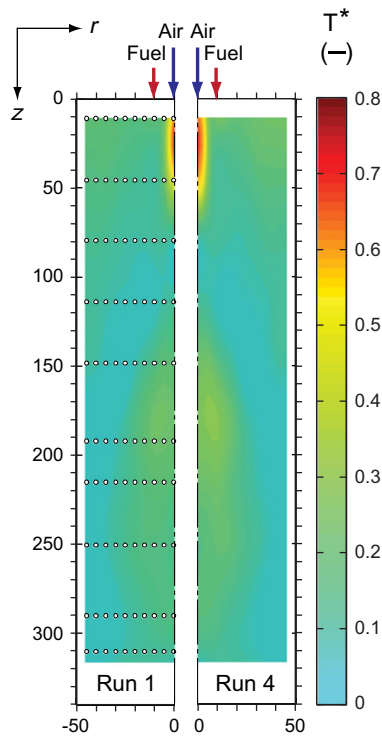


Fig. 6. Contours of normalized temperature variation ( $T^*$ ) at the combustor symmetry plane for runs 1 ( $V_{\text{air}} = 113.2$  m/s) and 4 (230.1 m/s).

crease of the  $\text{NO}_x$  concentrations along the combustor reaching a steady value very close to the combustor exit ( $z = 340$  mm). This suggests that some of the slowest reactions involved in the NO formation, typically those controlled by chemical equilibrium, reach their final state close to  $z = 340$  mm. It is well known that NO formation via the thermal mechanism is strongly inhibited under flameless combustion conditions. In addition, for the present conditions ( $\lambda = 1.3$ ), NO formation via the prompt mechanism is expected also to be insignificant [15]. Under these circumstances and given the absence of nitrogen in the fuel, the formation of NO via the  $\text{N}_2\text{O}$  intermediate mechanism is expected to have an important role in the present reacting flows.

Fig. 7 presents the combustion regime regions, in a  $\lambda \times$  air jet momentum diagram, identified in the present combustor operating with a thermal input of 10 kW and an inlet air temperature of 400 °C. The figure was constructed based on flame visibility,

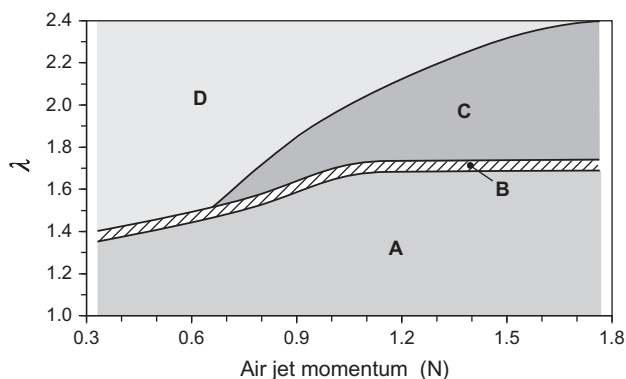


Fig. 7. Combustion regime regions identified in the present combustor operating with a thermal input of 10 kW and an inlet air temperature of 400 °C. (A) Flameless combustion, (B) transition region, (C) visible flame, and (D) No combustion.

$\text{OH}^*$  imaging,  $\text{NO}_x$  and CO emissions and in-combustor data (see also [3]). In common with previous work [e.g., 8,10,11], there is a critical central air jet momentum below which flameless combustion cannot occur in the present configuration. This critical minimum increases as  $\lambda$  increases up to 1.7, above which flameless oxidation cannot be established regardless of the air jet momentum. This suggests that the dilution of the reactants with a substantial amount of inert (flue) gases in configurations where the combustion air is provided by a central high-momentum air jet that is surrounded by a number of low-momentum fuel jets may cause difficulties to the application of the flameless technology to future gas turbines.

#### 4. Conclusions

The main conclusions from this investigation are as follows.

1. The  $\text{OH}^*$  images showed that as  $V_{\text{air}}$  increases at a constant  $\lambda = 1.3$ , the main reaction zone, typical of flameless combustion condition, remains approximately in the same region of the combustor, because of the flow aerodynamics similarity, but the  $\text{OH}^*$  intensities decrease, which indicates higher entrainment ratios of the fuel and burned gases by the central air jet.
2. For  $\lambda > 1.7$ , however, flameless oxidation could not be established regardless of the air jet momentum. This suggests that the establishment of the flameless combustion condition in future gas turbines through the dilution of the reactants with a substantial amount of flue gases in configurations where the combustion air is provided by a central high-momentum air jet that is surrounded by a number of low-momentum fuel jets may be problematic.

#### Acknowledgements

This work was developed within the framework of Project PTDC/EME-MFE/102997/2008, which is financially supported by Fundação para a Ciência e a Tecnologia (FCT). A.S. Veríssimo is pleased to acknowledge the Coordenação de Aperfeiçoamento de Pessoal de Nível Superior (CAPES) for the provision of the scholarship BEX:3909/05-0 and A.M.A. Rocha is pleased to acknowledge the FCT for the provision of the scholarship SFRH/BPD/40709/2007.

#### References

- [1] C. Duwig, B. Li, Z.S. Li, M. Aldén, High resolution imaging of flameless and distributed turbulent combustion, *Combust. Flame* 159 (2012) 306–316.
- [2] G. Li, E.J. Gutmark, D. Stankovic, N. Overman, M. Cornwell, L. Fuchs, M. Vladimir, Experimental Study of Flameless Combustion in Gas Turbines Combustors, in: 44th AIAA Aerospace Sciences Meeting and Exhibit, Paper no. AIAA 2006-546, Reno, Nevada, USA, 2006.
- [3] A.S. Veríssimo, A.M.A. Rocha, M. Costa, Operational, combustion and emission characteristics of a small-scale combustor, *Energy Fuels* 25 (2011) 2469–2480.
- [4] J.A. Wünnig, J.G. Wünnig, Flameless oxidation to reduce thermal NO-formation, *Prog. Energy Combust. Sci.* 23 (1997) 81–94.
- [5] A. Cavaliere, M. de Joannon, Mild Combustion, *Prog. Energy Combust. Sci.* 30 (2004) 329–366.
- [6] H. Tsuji, A.K. Gupta, T. Hasegawa, M. Katsuki, K. Kishimoto, M. Morita, *High Temperature Air Combustion*, CRC Press, 2003.
- [7] M. Mancini, P. Schwöppe, R. Weber, S. Orsino, On mathematical modelling of flameless combustion, *Combust. Flame* 150 (2007) 54–59.
- [8] M. Derudi, A. Villani, R. Rota, Mild combustion of industrial hydrogen-containing byproducts, *Ind. Eng. Chem. Res.* 46 (2007) 6806–6811.
- [9] P.R. Medwell, P.A.M. Kalt, B.B. Dally, Imaging of diluted turbulent ethylene flames stabilized on a jet in hot coflow (JHC) burner, *Combust. Flame* 152 (2008) 100–113.
- [10] G.G. Szegő, B.B. Dally, G.J. Nathan, Operational characteristics of a parallel jet MILD combustion burner system, *Combust. Flame* 156 (2009) 429–438.
- [11] J. Mi, P. Li, B.B. Dally, R.A. Craig, Importance of initial momentum rate and air-fuel premixing on moderate or intense low oxygen dilution (MILD) combustion in a recuperative furnace, *Energy Fuels* 23 (2009) 5349–5356.

- [12] E. Oldenhof, M.J. Tummers, E.H. van Veen, D.J.E.M. Roekaerts, Ignition kernel formation and lift-off behaviour of jet-in-hot-coflow flames, *Combust. Flame* 157 (2010) 1167–1178.
- [13] E. Oldenhof, M.J. Tummers, E.H. van Veen, D.J.E.M. Roekaerts, Role of entrainment in the stabilisation of jet-in-hot-coflow flames, *Combust. Flame* 158 (2011) 1553–1563.
- [14] J.G. Lee, D.A. Santavica, Experimental diagnostics for the study of combustion instabilities in lean premixed combustors, *J. Propul. Power* 19 (2003) 735–750.
- [15] A. Parente, C. Galletti, L. Tognotti, A simplified approach for predicting NO formation in MILD combustion of CH<sub>4</sub>–H<sub>2</sub> mixtures, *Proc. Combust. Inst.* 33 (2011) 3343–3350.